

# THE IMPACT OF PROGENITOR MASS LOSS ON THE DYNAMICAL AND SPECTRAL EVOLUTION OF SUPERNOVA REMNANTS

DANIEL J. PATNAUDE,<sup>1</sup> SHIU-HANG LEE,<sup>2</sup> PATRICK O. SLANE,<sup>1</sup> CARLES BADENES,<sup>3,4</sup> SHIGEHIRO NAGATAKI,<sup>5</sup>  
DONALD C. ELLISON,<sup>6</sup> AND DAN MILISAVLJEVIC<sup>1,7</sup>

<sup>1</sup>*Smithsonian Astrophysical Observatory, Cambridge, MA 02138, USA*

<sup>2</sup>*Kyoto University, Department of Astronomy, Oiwake-cho, Kitashirakawa, Sakyo-ku, Kyoto 606-8502, JP*

<sup>3</sup>*Department of Physics and Astronomy and Pittsburgh Particle Physics, Astrophysics and Cosmology Center (PITT PACC), University of Pittsburgh, 3941 O'Hara St, Pittsburgh, PA 15260, USA*

<sup>4</sup>*Institut de Ciències del Cosmos, Universitat de Barcelona (ICCUB), Martí i Franques 1, Barcelona, 08028, Spain*

<sup>5</sup>*RIKEN, Astrophysical Big Bang Laboratory & Interdisciplinary Theoretical and Mathematical Science Program, 2-1 Hirosawa, Wako, Saitama 351-0198, JP*

<sup>6</sup>*Department of Physics, North Carolina State University, Raleigh, NC 27695-8202, USA*

<sup>7</sup>*Purdue University, Department of Physics and Astronomy, 525 Northwestern Avenue, West Lafayette, IN 47907*

## ABSTRACT

There is now substantial evidence that the progenitors of some core-collapse supernovae undergo enhanced or extreme mass loss prior to explosion. The imprint of this mass loss is observed in the spectra and dynamics of the expanding blastwave on timescales of days to years after core-collapse, and the effects on the spectral and dynamical evolution may linger long after the supernova has evolved into the remnant stage. In this paper, we present for the first time, largely self-consistent end-to-end simulations for the evolution of a massive star from the pre-main sequence, up to and through core collapse, and into the remnant phase. We present three models and compare and contrast how the progenitor mass loss history impacts the dynamics and spectral evolution of the supernovae and supernova remnants. We study a model which only includes steady mass loss, a model with enhanced mass loss over a period of  $\sim 5000$  years prior to core-collapse, and a model with extreme mass loss over a period of  $\sim 500$  years prior to core collapse. The models are not meant to address any particular supernova or supernova remnant, but rather to highlight the important role that the progenitor evolution plays in the observable qualities of supernovae and supernova remnants. Through comparisons of these three different progenitor evolution scenarios, we find that the mass loss in late stages (during and after core carbon burning) can have a profound impact on the dynamics and spectral evolution of the supernova remnant centuries after core-collapse.

arXiv:1708.04984v1 [astro-ph.HE] 16 Aug 2017

## 1. INTRODUCTION

When interpreting the remnants of core collapse supernovae (CCSNe), assumptions regarding the isotropy of the progenitor mass loss are frequently made. Often times, it is assumed that the mass loss remained steady up to core collapse (c.f., [Chevalier 2005](#)). However, the endpoint in massive star evolution is poorly understood. In particular, violent and episodic mass loss is now observed in the progenitors of some core collapse supernovae (CCSNe), most notably in SN 2009ip ( $\dot{M} \sim 0.1 M_{\odot} \text{ yr}^{-1}$ ; [Pastorello et al. 2013](#); [Mauerhan et al. 2013](#); [Fraser et al. 2013](#); [Margutti et al. 2014](#); [Smith et al. 2014](#)), though substantial evidence exists for extreme mass loss in other Type IIn supernovae ([Ofek et al. 2013, 2014](#); [Elias-Rosa et al. 2016](#); [Smith et al. 2017](#)). More exotic mass loss is ascribed to Type Ibn SNe (e.g., SN 2006jc; [Pastorello et al. 2008](#)) and Type Ib/c SN that transition to Type IIn after some time, including SN 2001em ([Chugai & Chevalier 2006](#)), and SN 2014C ([Milisavljevic et al. 2015](#); [Margutti et al. 2017](#)). Even in “normal” SN I Ib/IIL and SN IIP, evidence for enhanced mass loss (relative to rates observed in red supergiants; [Smith 2014](#)) is observed (e.g., [Milisavljevic et al. 2013](#); [Maeda et al. 2015](#); [Kamble et al. 2016](#); [Chakraborti et al. 2016](#); [Morozova et al. 2017](#)).

The origin of the extreme mass loss remains a mystery, but several theories have been suggested. For instance, the onset of core carbon and oxygen burning can lead to stellar cores that are super-Eddington. Some of this energy could be tapped by as of yet poorly understood processes in the core ([Quataert & Shiode 2012](#); [Shiode & Quataert 2014](#)). If the progenitor is sufficiently compact, convectively driven waves could rise to the surface and unbind envelope material, depositing it into the circumstellar environment. Similarly, nuclear shell burning could lead to unstable flows near the surface, possibly also ejecting material on timescales that are short relative to the life of the progenitor ([Smith & Arnett 2014](#)).

On longer timescales, stable mass transfer or common envelope evolution could remove material from the surface of the progenitor ([de Mink et al. 2013](#)). In the case of a common envelope binary system, the H-rich envelope could be removed prior to core collapse (e.g., [Podsiadlowski et al. 1992](#)). Whatever the mechanism, evidence for enhanced mass loss prior to core collapse is observed, either directly through massive eruptions by so called supernova-impostors, or through the interaction of the blastwave with a circumstellar shell of ejected material, as in some IIn or even more typical IIP/IIL/I Ib supernovae.

As illustrated in [Figure 1](#), while supernovae sample the stages of evolution much closer to core collapse, super-

nova remnants (SNRs) typically probe stellar evolution on much longer timescales (c.f., [Patnaude & Badenes 2017](#)). This is because the timescale for the evolution of the circumstellar environment is set by the outflow speed of the wind, while the evolutionary timescale for the supernova remnant is determined by the blastwave velocity. For example, a  $10000 \text{ km s}^{-1}$  shock that expands into a  $10 \text{ km s}^{-1}$  wind samples 1000 years of stellar evolution for every year of blastwave evolution – a 100 year old SNR has probed a significant portion of the red supergiant (RSG) phase of a massive star’s life. This would imply that SNR shocks are not effective probes of the latter stages of stellar evolution, since they interact with material lost primarily during core helium burning.

However, while the characteristic timescale for SNR evolution is a few thousand years and is dependent upon the explosion energetics, ejecta mass, and circumstellar density ([Truelove & McKee 1999](#)), the timescale for ions and electrons to recombine in a partially ionized plasma is  $\sim 10^{12}/n_e$  s, where  $n_e$  is the number density of electrons. The circumstellar density around a massive star is generally thought to decrease with increasing radius due to flux conservation in the stellar wind ([Dwarkadas 2005, 2007](#); [Dwarkadas & Gruszko 2012](#)). So, as the supernova shock expands into the wind, the density of shocked material decreases, so that  $n_e$  is a decreasing function of SN age. This suggests that the recombination timescale in the plasma increases with increasing remnant age, and any circumstellar interaction that occurs early in the remnant evolution could be detectable at later remnant ages.

Often times, the X-ray spectrum from shocked circumstellar material is modeled as a blastwave interacting with a progenitor wind where the density  $\rho_{\text{CSM}} \propto r^{-2}$ . However, in [Patnaude et al. \(2015\)](#), we demonstrated that many SNRs do not always show X-ray emission that is consistent with the interaction between the ejecta and a power-law wind. We argued that enhanced mass loss prior to core collapse could greatly increase the X-ray luminosity without strongly affecting the blastwave radius. This is because the X-ray emission scales like the density squared, while the blastwave radius is only a weak function of the ambient medium.

In this paper, we extend [Patnaude et al. \(2015\)](#) by following the end-to-end evolution of a massive star, from the pre-main sequence, through the remnant phase. We accomplish this by using the MESA stellar evolution code to construct three different massive progenitor scenarios – one where the progenitor loses very little mass to a standard power-law wind; one where the star is stripped of some of its envelope during core carbon burning; and one where the H-envelope is almost entirely re-

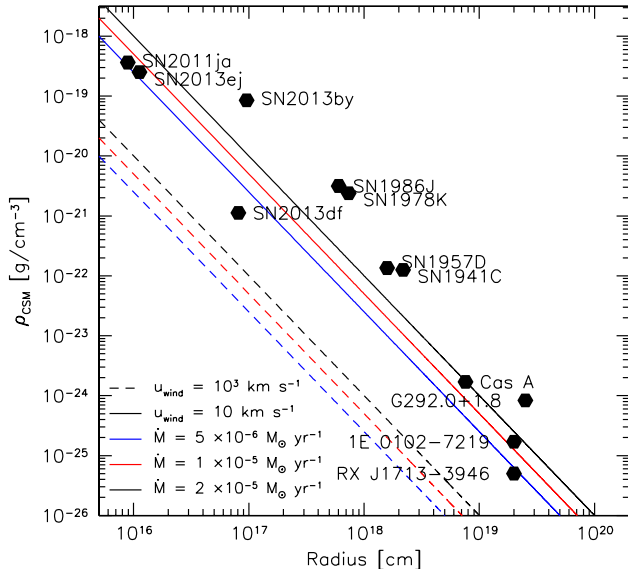


**Figure 1.** Comparison of SNe and SNR radii with those predicted via various mass loss rates and outflow speeds. The SNe/SNR radii can be related back to the time before core collapse, if assumptions about the shock speed and wind speed are made, since  $t_{\text{shock}} = v_{\text{wind}} \times t_{\text{wind}} / v_{\text{shock}}$ . For supernovae, radii are derived from the X-ray emission, assuming a wind speed of  $10 \text{ km s}^{-1}$  (Immler & Lewin 2003). Data are from Ross & Dwarkadas (2017); Long et al. (2012); Soria & Perna (2008). Data for supernova remnants are from Patnaude et al. (2009), Lee et al. (2010) and Ellison et al. (2012).

moved during core oxygen burning. We use the mass loss history of the progenitor to construct its circumstellar environment. Using a version of SNEC modified to follow the explosive nucleosynthesis that occurs during core collapse, we explode these progenitors, computing the velocity and density fields of the ejecta, as well as its composition. We follow the evolution of these models to ages of 400 year with our ChN code, simulating CSM properties appropriate for each mass loss scenario. In Section 2, we describe in detail each model component, and address the uncertainties associated with each model. In Section 3, we present and discuss our models. We present our conclusions in Section 4.

## 2. END-TO-END MODELS

In this section, we discuss the chain of models we use to simulate the stellar evolution up to, through, and beyond core collapse. In each subsection, we discuss the models used for each evolutionary stage. In the last subsection we discuss the uncertainties in our approach. We stress that no model is tailored to address any particu-

lar supernova or remnant, and that we are presenting a parametrized framework with which we can study more specific scenarios in the future.

### 2.1. Stellar Evolution Models

Models for  $15M_{\odot}$  progenitors are evolved using Modules for Experiments in Stellar Astrophysics (hereafter MESA, version 8845; Paxton et al. 2011, 2013, 2015)<sup>1</sup>. All models are initialized at solar metallicity ( $Z = 0.02$ ). We evolve three models, without rotation, but we employ the ‘‘Dutch’’ wind-scheme (Nieuwenhuijzen & de Jager 1990; Nugis & Lamers 2000; Vink et al. 2001; Glebbeek et al. 2009) with an efficiency  $\eta = 0.8$ . Each model is evolved from the pre-MS through core collapse, which we define as the time when the infall velocity at any location is  $\geq 1000 \text{ km s}^{-1}$ . For each model, we use MESA inlists made available from Farmer et al. (2016). We follow their scheme for specifying the mass and temporal evolution of the models during burning phases leading up to core collapse.

We make use of the `aprox21` nuclear burning network. This is chosen for (1) speed and efficiency, and (2) to match the burning network we have added to our supernova models (Section 2.2). While Farmer et al. (2016) concluded that the final electron fraction and mass locations of the primary nuclear burning shells can vary by  $\approx 30\%$  based on the choice of nuclear burning network, and that a minimum of 127 isotopes are needed in order to gain convergence in these values at levels of 10% or better, we note that we are interested in the bulk qualities of X-ray spectra from astrophysically abundant elements (O, Si, S, Fe, etc.). Additionally, since we are comparing the synthesized X-ray spectra amongst models and not making any comparisons of final elemental yields to observations – we feel that our choice of nuclear burning network satisfies our requirement for speed and efficiency while also capturing the spirit of the necessary physics.

We specify three models. Model `m15Iso` uses the Dutch wind models up to the onset of core collapse. The average mass loss rate over the lifetime of the star is  $\sim 5 \times 10^{-6} M_{\odot} \text{ yr}^{-1}$ . Model `m15C` includes enhanced mass loss during core carbon burning, at a constant rate of  $10^{-4} M_{\odot} \text{ yr}^{-1}$ , resulting in  $\sim 2$  additional solar masses of material deposited into the circumstellar environment. When core oxygen burning begins, we revert to mass loss rates from the Dutch scheme. Model `m15O` follows isotropic mass loss up to core oxygen burning, at which point we employ extreme mass loss. In this case, the mass loss is held fixed at  $0.1 M_{\odot} \text{ yr}^{-1}$ .

<sup>1</sup> <http://sourceforge.mesa.net>

We include this extreme mass loss until the formation of the silicon core. During this phase, the progenitor loses  $\sim 6M_{\odot}$  of material. At the onset of core collapse, our models have final masses of  $\sim 13$ ,  $10$ , and  $6M_{\odot}$ .

We stress that the enhanced and extreme mass loss models are not meant to represent any physical processes associated with late stage stellar evolution. While there is growing evidence for enhanced mass loss in supernova progenitors prior to core collapse, both on timescales of  $\sim$  a few thousand years, down to timescales of a few years, the mechanism for this mass loss remains poorly understood, and could result from hydrodynamic instabilities and turbulence in the outer layers of the star (Smith & Arnett 2014), wave-driven mass loss due to energy extraction from the super-Eddington core (Quataert & Shiode 2012; Shiode & Quataert 2014), or pulsational-driven superwinds (Yoon & Cantiello 2010) amongst other possibilities. In this study, we are aiming to deposit the mass in the CSM at a position that is self-consistent with the timing of the mass loss epoch.

While the exact mass loss mechanism will undoubtedly alter the final evolution of the progenitor, we look to understand how the mass loss affects the evolution of the SNR, independent of how it arose. In Table 1, we present the initial and final parameters for each model, while in Figure 2, we plot the density and temperature of the progenitors for each model at the onset of core collapse. Beyond the large differences in final mass, brought about by the choice of fiducial mass loss, there are not large differences in the final parameters of the progenitors, with the most notable differences being in the final progenitor radii. As seen in Figure 2, the thermodynamic profile of the progenitor interior of  $\approx 6R_{\odot}$  are virtually identical. However, since nuclear reaction rates are sensitive to changes in temperature and density, it is these small differences that can lead to differences in the final compositions. Likewise, these small differences could lead to larger differences in the structure of the ejecta. For instance, the amount of envelope retained by the progenitor prior to core collapse could affect the growth of instabilities during the explosion (c.f., Wongwathanarat et al. 2015).

## 2.2. Supernova Models

The MESA models are coupled to a spherically symmetric (1D) Lagrangian hydrodynamics code that uses equilibrium-diffusion radiation transport. The code, called the SuperNova Explosion Code (hereafter referred to as SNEC<sup>2</sup>) is made freely available, and in its publicly available form, follows the time dependent radia-

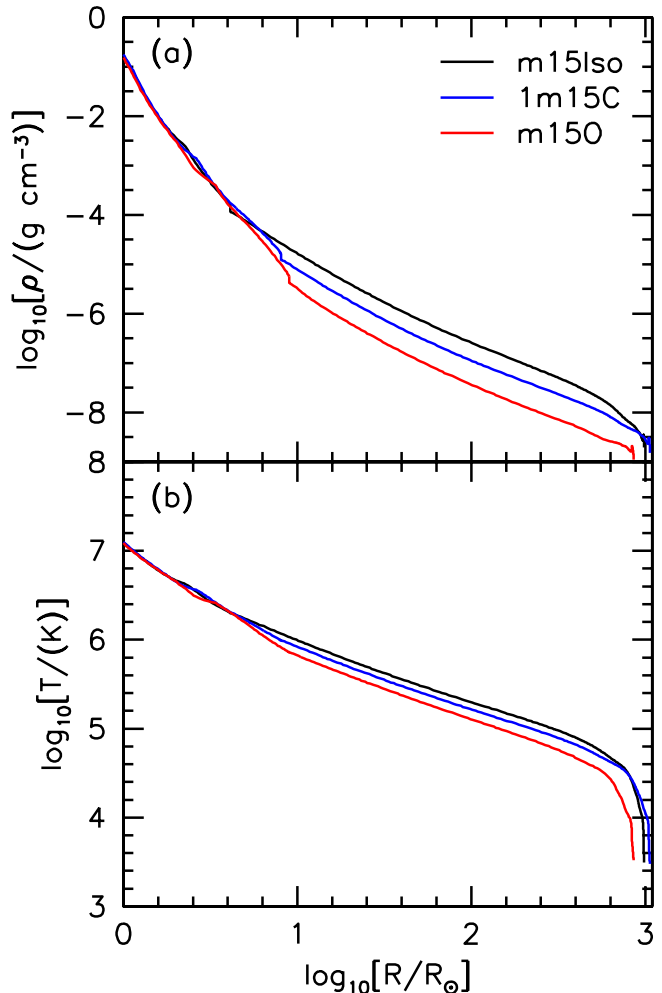


**Figure 2.** *Upper:* Density as a function of stellar radius for each model at the onset of core collapse. *Lower:* Final temperature for each model.

tion hydrodynamics and other basic physics needed for supernova light curve generation and  $^{56}\text{Ni}$  heating. A detailed discussion of SNEC may be found in Morozova et al. (2015); Piro & Morozova (2016); Morozova et al. (2017).

In its basic form, SNEC couples to a model for the structure and composition of the supernova progenitor. It includes the ability for an arbitrary composition, and includes a prescription for mixing of ejecta, via a box-car smoothing algorithm. Observations of supernovae and remnants show evidence for both mixing of Ni-rich ejecta during the explosion (e.g., SN 1987A; Li et al. 1993), as well as evidence for Rayleigh-Taylor mixing between layers of differing composition and densities, and these effects are confirmed in multidimensional numerical modeling of core collapse SNe during the first few seconds of evolution (Janka 2012; Wongwathanarat et al.

<sup>2</sup> <http://stellarcollapse.org/SNEC>

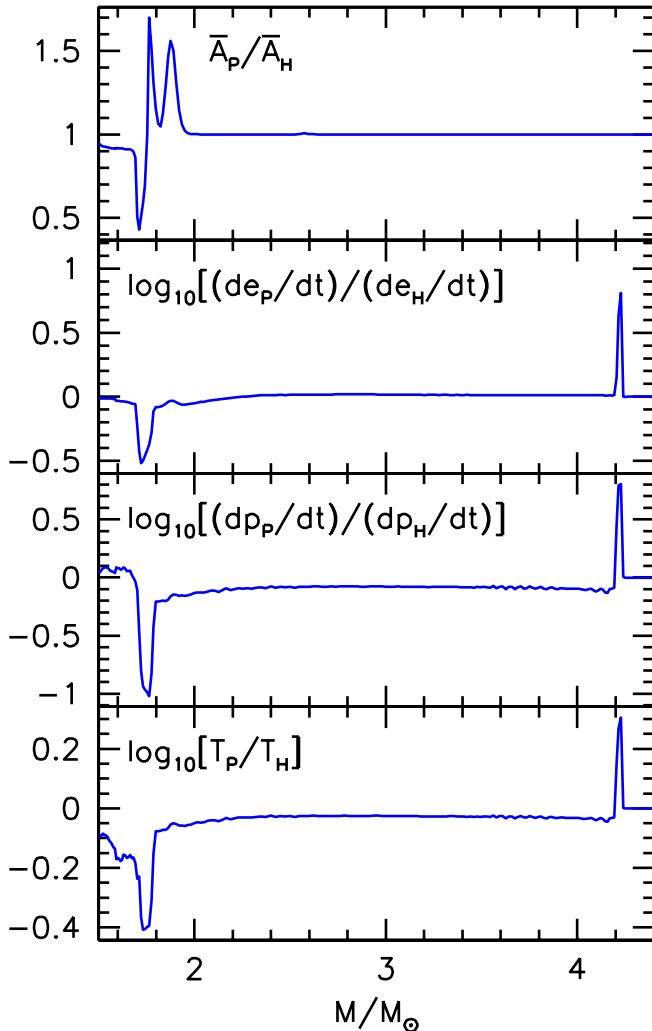


**Figure 3.** Differences between the Paczynski and Helmholtz Equations of State. The top panel shows differences in  $\bar{A}$  (the mean atomic mass), the middle two panels show differences in the time derivatives of internal energy and pressure, and the bottom panel shows differences in the temperature.

2015, 2017). While an approximation for the Rayleigh Taylor instability exists in one dimension (Duffell 2016), for this study we choose to ignore the mixing of metal-rich ejecta into the outer layers of the progenitor. As substantial evidence exists for the mixing of Ni and Fe-peak elements into the outer layers of ejecta, in both supernovae and some supernova remnants, we will explore mixing in followup papers.

SNEC allows the user to choose between either a thermal bomb or piston driven explosion. We choose to use the thermal bomb method, whereby we specify the core mass to be excised, and then energy is deposited in a user-specified number of mass zones, at which point the explosion calculation begins. This is a completely *ad-hoc*

method and ignores the important fact that the explosion is likely driven by a combination of neutrino heating of the shock and hydrodynamical instabilities.

Finally, SNEC closes the system of hydrodynamic conservation laws with the choice of an equation of state (EOS). The choices are either an ideal gas, or the Paczynski EOS (Paczynski 1983), which includes contributions to the total pressure from radiation, ions, and electrons. While the Paczynski EOS may provide a rough approximation, it is not thermodynamically consistent, does not treat pair-production, does not use a chemical potential, and is not suitable for an arbitrary composition<sup>3</sup>. Based on these limitations, we chose instead to incorporate the Helmholtz EOS (Timmes & Swesty 2000)<sup>4</sup>. The Helmholtz EOS is thermodynamically consistent. In Figure 3, we plot thermodynamic quantities and their derivatives as a function of mass coordinate in SNEC. The calculations shown in Figure 3 are for after explosive nucleosynthesis ceases. The largest differences, of order 0.5 dex, occur at both the location of the shock, and in areas just above the explosion launch point. Differences between the two EOS are most readily seen as small differences in the temperature of the shocked material, as well as differences in the pressure derivative. Nuclear burning is sensitive to the temperature, so anomalous heating due to an imprecise EOS can lead to extra burning in the ejecta. This is seen as a difference in  $\bar{A}$  in the top panel of Figure 3.

As mentioned, SNEC allows for arbitrary composition, but it does not include a way to update the composition due to explosive burning. Certainly, the additional nucleosynthesis during the explosion will not impact the observable properties of swept up material from the CSM interaction, but it could alter the measured abundances in the ejecta. We have chosen to implement nuclear burning by using the `approx21` network<sup>5</sup>. This is the same network we use in our MESA models, and is an adequate, yet incomplete burning network. For efficiency, we follow the burning in each mass shell until the temperature falls below  $10^7$  K. As discussed in Farmer et al. (2016), the final composition is sensitive to the nuclear reaction network chosen. We defer a study of larger networks to subsequent papers.

For each presupernova model, we assume an explosion energy of  $10^{51}$  erg. We choose to excise the inner  $1.5M_{\odot}$  (the approximate mass of the iron core; Table 1) from the progenitor model, and spread the energy across  $0.1M_{\odot}$  of ejecta, corresponding to a radial distance of  $\approx$

<sup>3</sup> Timmes; private communication

<sup>4</sup> [http://cococubed.asu.edu/code\\_pages/eos.shtml](http://cococubed.asu.edu/code_pages/eos.shtml)

<sup>5</sup> [http://cococubed.asu.edu/code\\_pages/burn.shtml](http://cococubed.asu.edu/code_pages/burn.shtml)

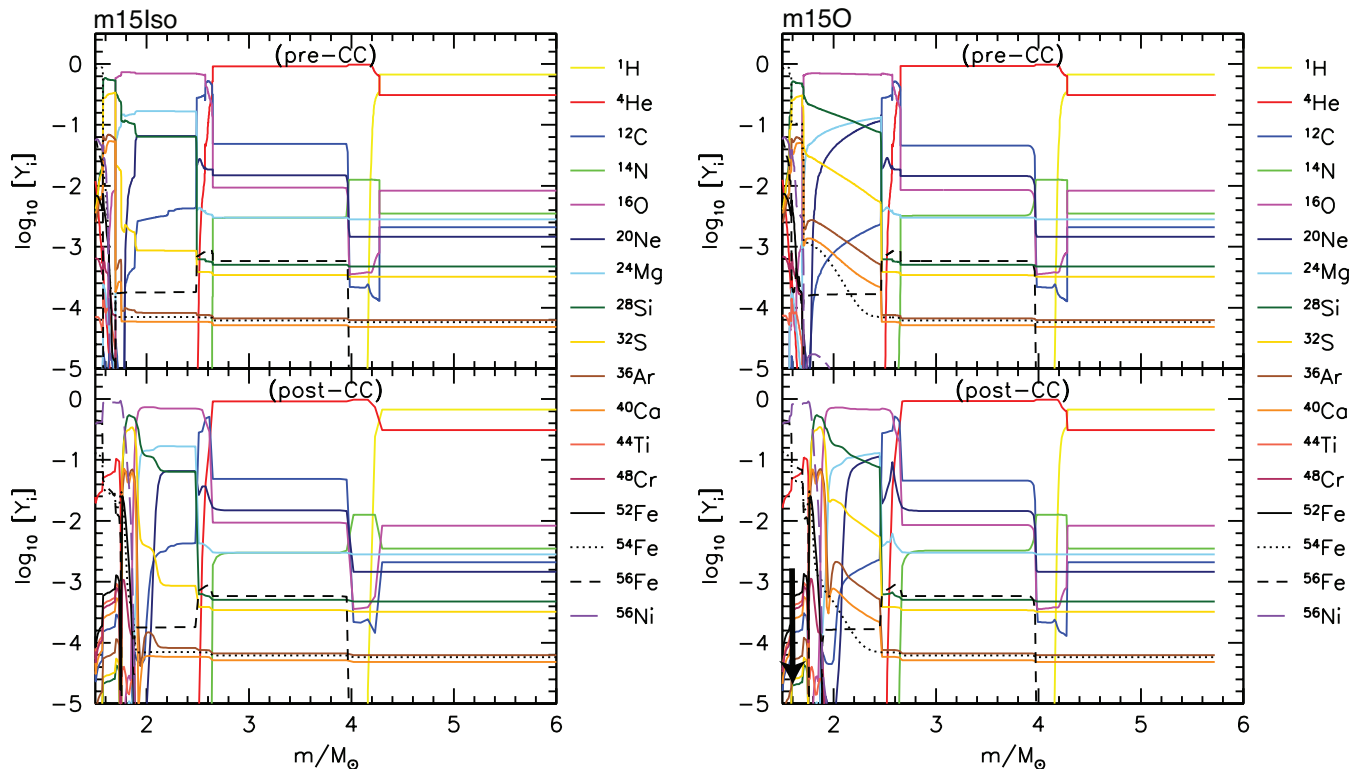


**Figure 4.** *Left:* Composition profile for the  $15M_{\odot}$  model with steady mass loss (m15Iso). The upper panel shows the composition of the inner  $6M_{\odot}$  prior to core collapse, while the lower panel shows the composition for the same elements after core collapse. There is no mixing assumed in these models. *Right:* Same as in the left-hand panel, but for the model that underwent extreme mass loss during core oxygen burning (m150). After evolving the models in the lower panels for 400 years with our ChN code,  $\sim 1M_{\odot}$  of ejecta are shocked in the isotropic wind model, while nearly all the ejecta in the highly stripped model are shocked, as indicated by the arrow in the bottom righthand panel.

200 km above the proto-neutron star. The energy deposition lasts for 100 ms. In multidimensional studies, typical core bounce timescales are 100–200 ms (c.f., Ott et al. 2008), so our choice of 100 ms is appropriate. The final composition and structure of the ejecta are both sensitive to the explosion energetics, but we chose values that are typical for core collapse supernovae, and consistent with 1D models of this type (Morozova et al. 2015). The explosion is followed to an age of 100 days.

We plot in Figure 4 the initial and final compositions for two of the models (m15Iso and m150). As seen in these plots, the composition of the models both pre and post core collapse are similar. In both models, and in model m15C which is not shown, the chemical compositions of the He-rich shell, located between mass coordinates of approximately  $2.6$  and  $4.2M_{\odot}$  are virtually identical, as are the compositions of the H-rich shell, exterior of  $4.2M_{\odot}$ . The differences in the models are how far the H-rich shell extends. Interior of the He-rich shell, differences in composition exist in the O-rich shell between  $1.8$  and  $2.6M_{\odot}$ , but these differences are likely due to differences that arise during the stellar evolution.

Interior to this, the compositions appear identical. It is not entirely surprising that the compositions are so similar, since the same explosion conditions are applied to all three models. It is worth noting that the differences in the EOS seen in Figure 3 correspond with locations of shell boundaries. The difference around  $4.2M_{\odot}$  corresponds to the boundary between the He- and H-rich layers, and the difference around  $1.8M_{\odot}$  between the O-rich and Si-rich layers. Differences in the EOS calculation appear insensitive to the boundary between the O-rich and He-rich layers.

We do not report explicitly the final composition in our models (see section 2.5). However, each model produces  $\lesssim 0.2M_{\odot}$  of  $^{56}\text{Ni}$ , and  $2 \times 10^{-4}M_{\odot}$  of  $^{44}\text{Ti}$ . Additionally, we estimate  $\sim 0.5$ – $0.8 M_{\odot}$  of silicon, and  $2$ – $3 M_{\odot}$  of oxygen are in the final ejecta models.

### 2.3. Circumstellar Models

In general terms, the circumstellar environment is dictated by the mass loss of the progenitor, and the wind velocity of the lost material. Neither parameter is completely constrained by observation (for a recent review,

see Smith 2014). Velocities can vary from as little as  $10 \text{ km s}^{-1}$  in a RSG, to  $\gtrsim 1000 \text{ km s}^{-1}$  in a Wolf-Rayet star. Mass loss rates can vary from  $\sim 0.1\text{--}10 M_{\odot} \text{ yr}^{-1}$  in a Luminous Blue Variable eruption, to as low as  $10^{-7} M_{\odot} \text{ yr}^{-1}$  in a Helium star<sup>6</sup>, and binary interactions and rotation can act to further enhance the mass loss.

As discussed in Section 2.1, we assume three mass loss scenarios. (1): a steady wind up to core collapse; (2): the onset of a fast wind with substantial mass loss during core carbon burning. This wind expands into the slower red supergiant wind that evolves in the CSM during hydrogen and helium burning, and persists for  $\sim 5000$  years, and the star loses a few solar masses of material; (3): extreme mass loss during core neon and oxygen burning. This phase lasts for  $\sim 500$  years; the star loses  $\sim 6 M_{\odot}$  of material during this phase.

MESA does report the mass loss as a function of time, and the mass loss is observed to vary with each timestep. This is entirely expected, as it is a derived quantity from other stellar parameters which are also functions of time. However, the dominant timescale in the CSM is the cooling time of swept-up shocked CSM,  $\sim 20$  years. This can be much longer than the relevant timescale in MESA, which is driven by the core burning and is  $\sim$  a few years during carbon burning, and of order seconds during oxygen burning. In light of this, we adopt a hybrid approach.

We model the CSM as a power law wind which is formed by the progenitor during H- and He-burning. This forms the CSM into which we evolve the other models, and to which we compare the other models. For the isotropic wind model, we adopt an average  $\dot{M} \approx 5 \times 10^{-6} M_{\odot} \text{ yr}^{-1}$ , with a wind speed of  $15 \text{ km s}^{-1}$ . This is the average value derived from MESA output, over the life of the star. This wind will form a shell of cooled, swept up ISM, but we estimate that for an initial ISM density of  $0.3 \text{ cm}^{-3}$ , the shell radius is  $\gtrsim 3.5 \text{ pc}$  for the 1.5 Myr evolution of the main sequence and helium burning phases, well beyond where the SNR shock will be after the 400 year post explosion evolution explored in this paper.

We model the enhanced and extreme mass loss cases in similar manners. We evolve these two cases into the steady wind produced during the earlier phases of evolution. Model m15C is evolved with a mass loss rate of  $10^{-4} M_{\odot} \text{ yr}^{-1}$  and a velocity of  $1000 \text{ km s}^{-1}$  until the core carbon abundance is depleted below  $10^{-3}$ . Model m150 is evolved with a mass loss rate of  $0.1 M_{\odot} \text{ yr}^{-1}$  and a velocity of order the progenitor escape velocity,  $\sim 100$

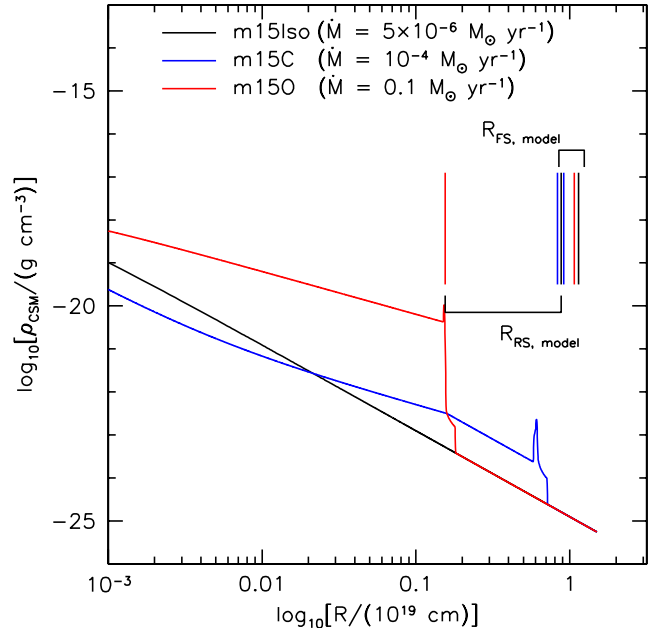


**Figure 5.** Circumstellar environments for each progenitor model prior to the remnant evolution. The black curve shows the CSM for model 15mISO, while the blue curve corresponds to model 15mC and the red curve to model 15m0. To accentuate the differences in the structure of the environment, we plot the base-10 logarithm of the radius. The final position of the SNR forward shock for each model is labeled. The curvature in model 15mC is a result in a ramp down in the mass loss rate  $\approx 1000$  years before the end of the simulation.

$\text{km s}^{-1}$ . For both cases, we assume a rise time in the wind of 10 years. For model m15C, we model the subsequent evolution after core carbon burning with a steady wind with mass loss rates  $10^{-5} M_{\odot} \text{ yr}$  and a wind velocity of  $10 \text{ km s}^{-1}$ . For model m150, the extreme mass loss persists until the onset of core silicon burning, which is a short enough phase that another mass loss model is not employed.

We use the numerical hydrodynamics code VH-1 (Blondin & Lufkin 1993) to model the evolution of the wind. VH-1 is a multidimensional general purpose hydrodynamics code which also forms the basis of our cosmic-ray hydrodynamics code (Ellison et al. 2007). For the purposes of modeling the CSM, we have included a routine to follow radiative losses in the shocked, swept up CSM, using both collisional and non-equilibrium ionization curves from Sutherland & Dopita (1993).

The density profiles of the modeled circumstellar environments are shown in Figure 5. While the isotropic case follows the standard  $\rho_{\text{CSM}} \propto r^{-2}$ , a radiatively cooled CSM shell forms in the case of the  $10^{-4} M_{\odot} \text{ yr}^{-1}$  wind. However, in the extreme mass loss case, the shell does

<sup>6</sup> Velocities and mass loss rates are taken from Table 1 of Smith (2014)

not cool radiatively before the simulation ends. In this case, the progenitor will explode within a few days of the exhaustion of the oxygen core. For reference, we mark the positions of the forward and reverse shocks at  $t_{\text{SNR}}$  for each model of SNR evolution, discussed in the next section.

#### 2.4. Remnant Evolution Models

Lastly, we model the evolution of the ejecta discussed in Section 2.2 into circumstellar profiles discussed in Section 2.3. We use our cosmic ray hydrodynamics code, hereafter called **ChN** to model the evolution of the ejecta to an age of  $t_{\text{SNR}} = 400$  yr. **ChN** is a Lagrangian hydrodynamics code that includes a prescription for diffusive shock acceleration (DSA; Ellison et al. 2007; Lee et al. 2012). We have modified the code to include the effects of DSA on non-equilibrium ionization (Patnaude et al. 2009, 2010) and have coupled the code to supernova ejecta models (Lee et al. 2014; Patnaude et al. 2015). We have also included radiative losses via forbidden line cooling (Lee et al. 2015). This effect will be important in the evolution of the SN shock with a nearby CSM shell, or if we choose to model the radiative shock that could form in the ejecta during early supernova evolution (Nymark et al. 2006). However, we begin our simulations at an age of 5 years, and over the lifetime of the simulation the shocks remain adiabatic, so we do not consider the radiative shock model presented in our previous work here. Since **ChN** couples nonlinear particle acceleration to the SNR shock dynamics, we are able to reproduce the broadband thermal and nonthermal emission (Ellison et al. 2010, 2012; Castro et al. 2012; Slane et al. 2014; Lee et al. 2013). The diffusive shock acceleration process is an integral part of **ChN**, and some injection of thermal particles into the acceleration process is always assumed. Here we set the injection parameter to the test particle limit, though we note that the interaction of a strong shock with a massive CSM shell or cloud will lead to enhanced particle acceleration (e.g., Ellison et al. 2012; Lee et al. 2014), and the differing CSM configurations, combined with the differing ejecta profiles and compositions, may result in differences in the broadband nonthermal emission. The study of nonthermal emission in evolving supernovae is sufficiently broad that we defer its study to future papers.

We simulate the SNR shock evolution to an age of 400 years. Using the time-dependent ionization balance, we compute the thermal X-ray emission from the shocked CSM and ejecta. **ChN** has the capability to compute spectra from APED (Foster et al. 2012), or from a more primitive X-ray emission code discussed in Patnaude et al. (2010). While our previous studies have made use

of the code discussed in Patnaude et al. (2010), we feel that the more thorough treatment provided by APED will make our simulations accessible to future high-resolution X-ray spectroscopy missions. In Figure 6, we plot the final profile of each model after 400 years. We also plot the final average charge state for oxygen, silicon, and iron.

We plot the evolution of the synthetic X-ray spectra from each model in Figures 7–8. We have assumed an SNR distance of 1 kpc. The spectra have been both thermal and Doppler broadened (Lee et al. 2014), and for clarity, we do not include the effects of interstellar absorption, which can be significant below 1 keV.

#### 2.5. Model Uncertainties

While we are not aiming to model any particular remnant in detail, each component of the model chain has uncertainty associated with both the input data and the chosen physics. Statistical uncertainty in measured nuclear and atomic cross sections are discussed in detail in their original source papers, referred to in the preceding subsections. Here we aim to understand the uncertainty that is inherent in our choice of input physics and parameters. We qualitatively summarize the uncertainty below.

For our stellar evolution models, we do not account for rotation or magnetic fields, and we choose a limited nuclear reaction network. The choice of nuclear reaction network can impact the final abundances of key elements such as oxygen and silicon in the core at core collapse by as much as 30% (Farmer et al. 2016). The exact details of the mass loss mechanism remain poorly understood (Smith 2014). The mass loss rates we choose, both the quasi-steady rate in the isotropic model, as well as the enhanced rates span a parameter space that is broadly consistent with observed rates for steady and episodic mass loss, but given the one-dimensional nature of our models, do not account for effects such as clumping in the wind. Additionally, we have smoothed the CSM density with a Gaussian kernel in an attempt to smear out the sharp transitions that occur around the CSM shell boundary. In reality, the transition between the powerlaw wind and the CSM shell may be more complicated.

In the explosion phase of our modeling, the choice of mass cut, thermal bomb duration, and bomb spread can all affect the nucleosynthesis. Young & Fryer (2007) studied variations in nucleosynthetic yields in one-dimensional explosion models and came to the conclusion that high- $Z$  element production is sensitive to the explosion energy, and that yields may differ by as much as 50% between thermal bomb and piston driven



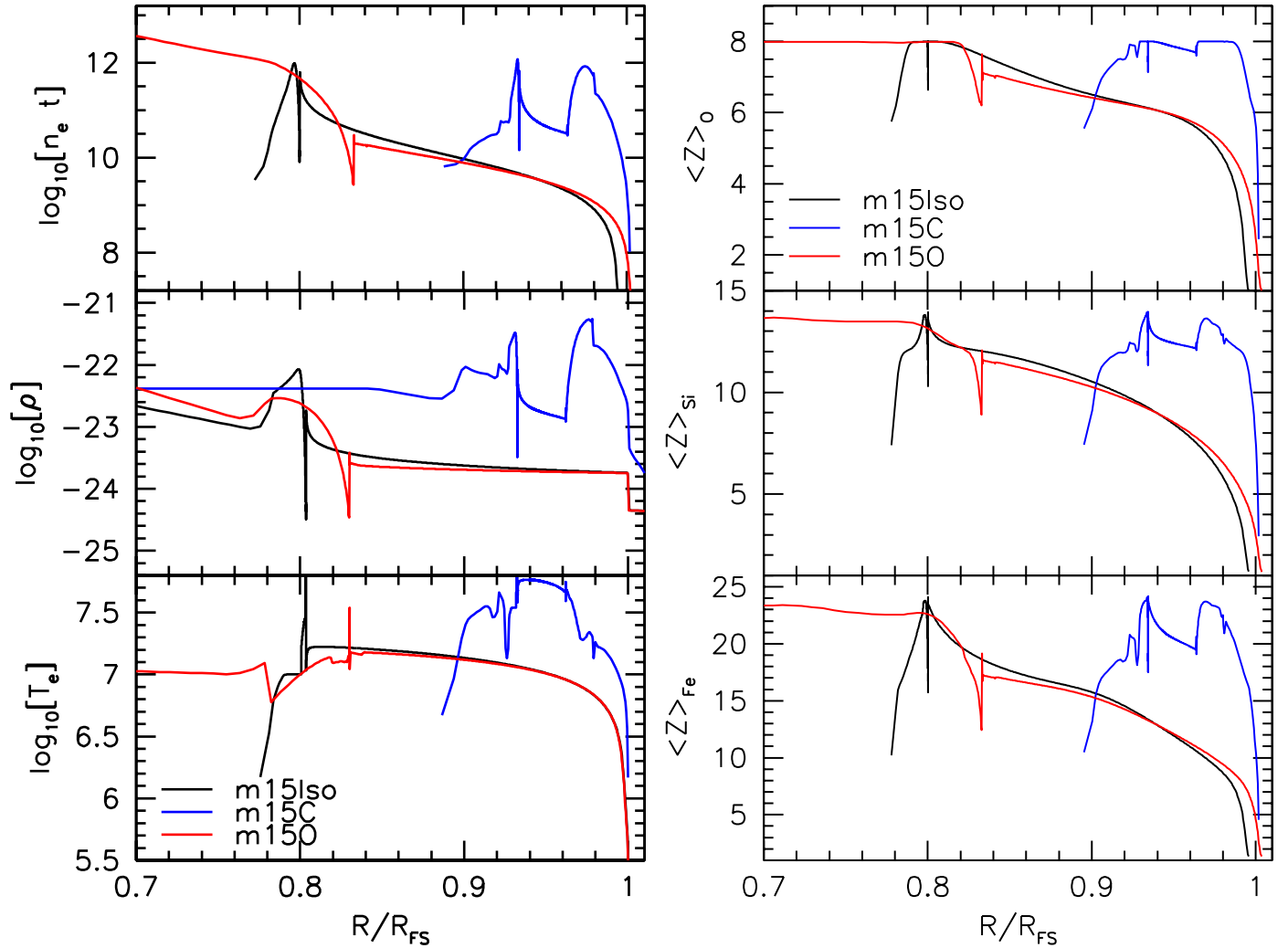


**Figure 6.** *Left:* Hydrodynamical state of each model after 400 years of evolution. The top and bottom panels show the ionization age ( $n_e t$ ) and electron temperature ( $T_e$ ) of shocked material only, while the middle panel shows the density for shocked and unshocked material. The temperature spikes seen in the plot of  $T_e$  are due to contact discontinuities in the 1D model. These spikes coincide with regions of low density and thus do not contribute to the overall emission. *Right:* Average charge state for oxygen (top), silicon (middle), and iron (bottom).

explosions. In essence, the yields are non-unique for a given progenitor, and can vary based on how the energy is deposited in the progenitor. The progenitor masses at core collapse differ for our three models, though we choose the same explosion energy, bomb spread, and heating duration. Since the nucleosynthesis is sensitive to this and the core density and composition, and since these do not vary across the three models by much, the final abundances interior of the helium core are very similar, with each producing  $\lesssim 0.2 M_\odot$  of  $^{56}\text{Ni}$ . A more dynamic reaction network would probably lower this nickel mass by quite a bit (Young & Fryer 2007), though  $0.2 M_\odot$  of  $^{56}\text{Ni}$  is consistent with yields expected from some core collapse supernova models (Young & Fryer 2007). For the remnant modeling, we do not consider non-linear

shock acceleration effects, which can alter the dynamics and emitted spectrum (Ellison et al. 2007; Patnaude et al. 2011; Lee et al. 2012).

Finally, we comment on the limitations of our one-dimensional modeling. As discussed above, we don't include the effects of rotation in the stellar evolution modeling. This can alter the mixing between layers and the treatment of convection during the stellar evolution. In the CSM, 1D models result in CSM shells, instead of a web of tenuous wind peppered by condensed clumps. For the explosion and remnant evolution modeling, 1D models are unable to follow the effects of mixing due to the Rayleigh-Taylor (RT) or Kelvin-Helmholtz instabilities. Duffell (2016) recently presented a prescription for the 1D RT instability, and we will incorporate these

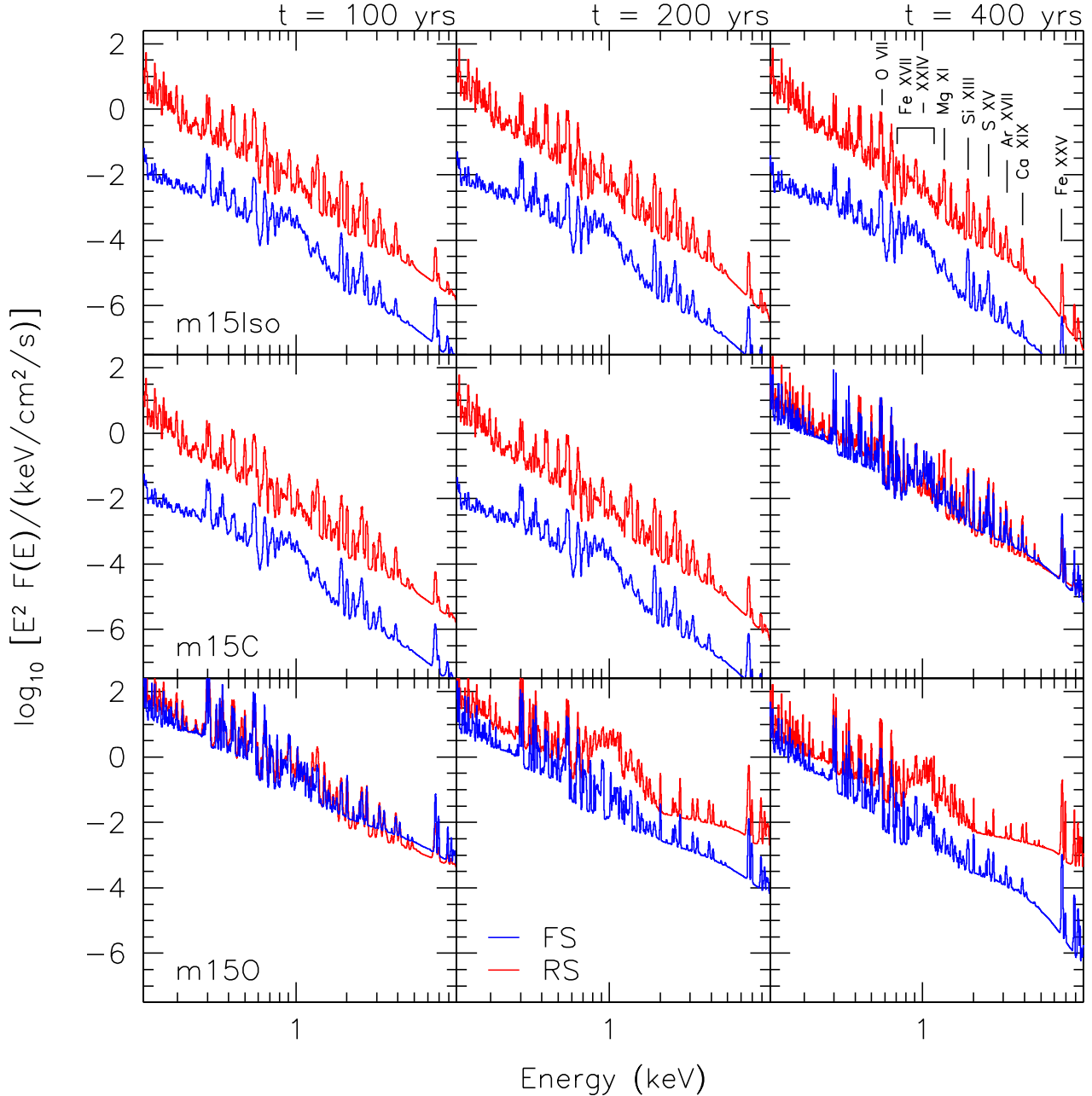


**Figure 7.** Simulated X-ray spectra from the forward and reverse shock for models m15Iso, m15C, and m150, at ages of 100, 200, and 400 years. Bright He-like lines and lines from Fe XVII–Fe XXIV are marked in the top right panel.

effects in subsequent studies. We have also not included the bulk mixing of ejecta via convective instabilities during the explosion. This will alter the abundances in the outer layers of the star, resulting in changes to the emitted X-ray spectrum from the ejecta.

Our models represent a first attempt to follow the complete evolution of a massive star from the pre-main sequence through the remnant phase. Each phase of

evolution takes as input parameters derived from a prior stage, allowing for a quasi self-consistent study of how massive star evolution affects the remnants we observe today. As is clear from the uncertainties discussed in this section, an end-to-end supernova simulation requires a number of approximations and assumptions. Nevertheless, we show below that meaningful constraints on

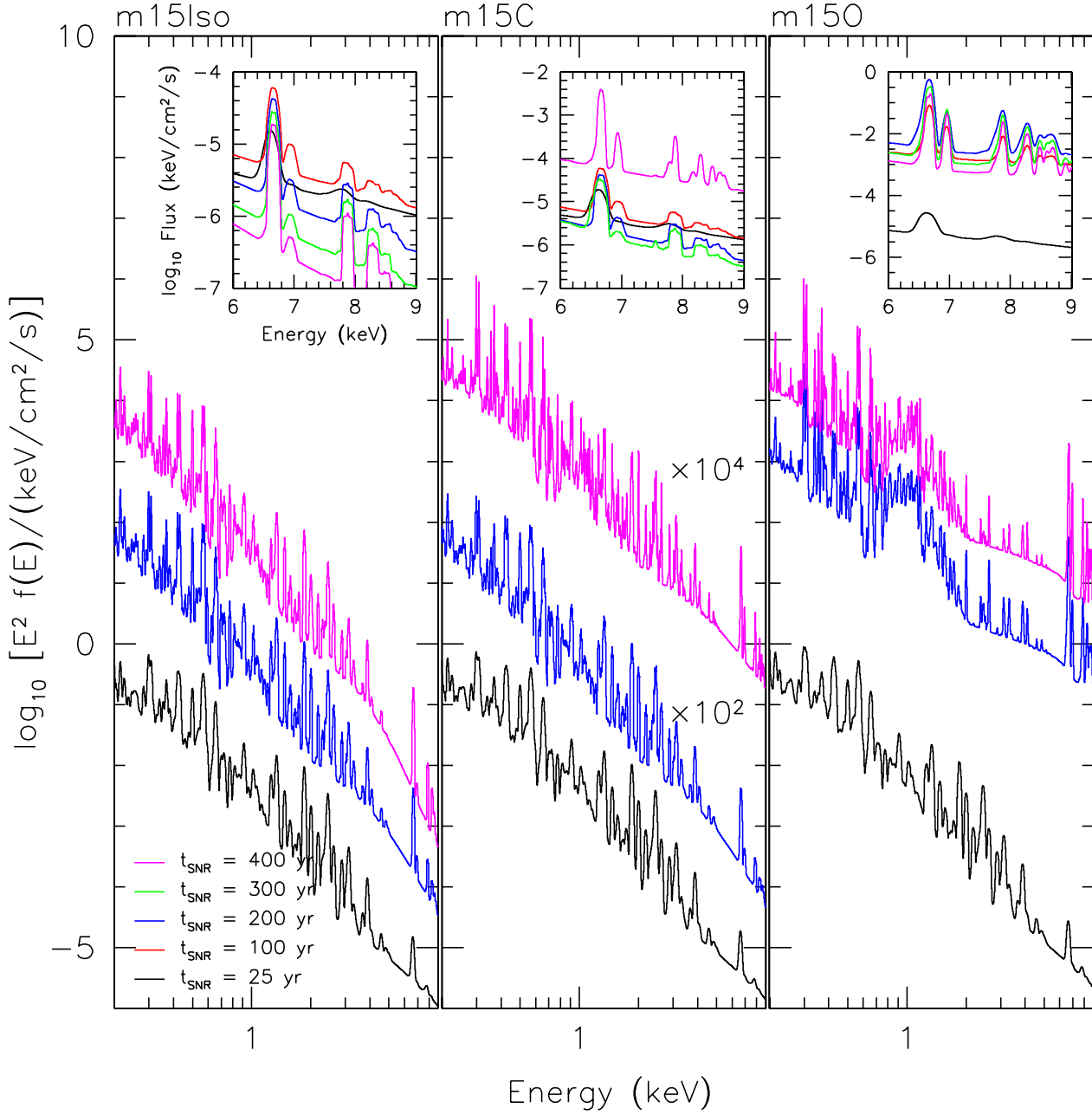


**Figure 8.** Integrated X-ray spectra for each model at ages between 25 and 400 years. In the main panels we plot the spectra at ages of 25, 200, and 400 years. The spectra at 200 and 400 years are scaled relative to the spectra at 25 years. The evolution of emission around Fe-K is shown in the insets, and represent absolute fluxes. We plot the evolution of the Fe-K emission at 25, 100, 200, 300, and 400 years.

the “hidden” supernova properties can be deduced from SNR observations made centuries after the explosion.

### 3. MODELING RESULTS AND DISCUSSION

The principal output from ChN includes the blastwave dynamics, as well as the broadband thermal and non-thermal emission. The results of our simulations are summarized in Table 2. For each model, we list the swept up mass and blastwave radius, the amount of shocked ejecta, and the bulk energy centroid for the He-like state of iron. We discuss the dynamical and spectral results below.

#### 3.1. Model Differences

As seen in Table 2, after 400 years, the blastwave radii for models **m15Iso** and **m150** are virtually identical, despite different stellar evolutionary histories. On the otherhand, model **m15C** is  $\sim 15\%$  smaller over the same time period. The positions of the forward shock, relative to the CSM are shown in Figure 5.

The blastwave radii are similar for **m15Iso** and **m150**, but the amount of swept up mass and shocked ejecta are remarkably different. **m15Iso** has swept up less than a solar mass of material in 400 years, and only shocked  $\sim 2 M_{\odot}$  of ejecta in that time. In contrast, in **m150** the blastwave has shocked  $\sim 8M_{\odot}$  of CSM material, and has progressed all the way into the center of the ejecta. Model **m15C** represents an intermediate case, in that it has shocked about 2 and  $6M_{\odot}$  of CSM and ejecta material, respectively. Spectra from shock heated CSM and ejecta for each model are shown in Figure 7, for ages of 100, 200, and 400 years, and differences in the amount of shocked material are readily apparent.

As seen in Figure 7, the spectral evolution for models **m15Iso** and **m15C** are virtually identical over the first 200 years of their evolution. At an age of 400 years, however, differences in their evolution become apparent, as the forward shock in model **m15C** interacts with the CSM shell (at  $\approx t_{\text{SNR}} = 230$  yr), and emission from shocked ejecta becomes comparable to that of shocked CSM. In contrast, at 100 years, the emission from shocked ejecta and shocked CSM are comparable in model **m150**. In this model, the shock interacts with the CSM shell at  $\approx 40$  years, and breaks out  $\approx 100$  years later. By 200 years, the forward shock is well into the lower density pre-shell wind, so the emission from swept up CSM begins to drop, due to adiabatic expansion.

As listed in Table 2, both models **m15C** and **m150** have swept over a comparable amount of ejecta. However, the composition of the shocked ejecta is quite different. At the time of core collapse, model **m15C** still has a H-rich envelope of mass  $\sim 8M_{\odot}$ . The H-rich envelope for

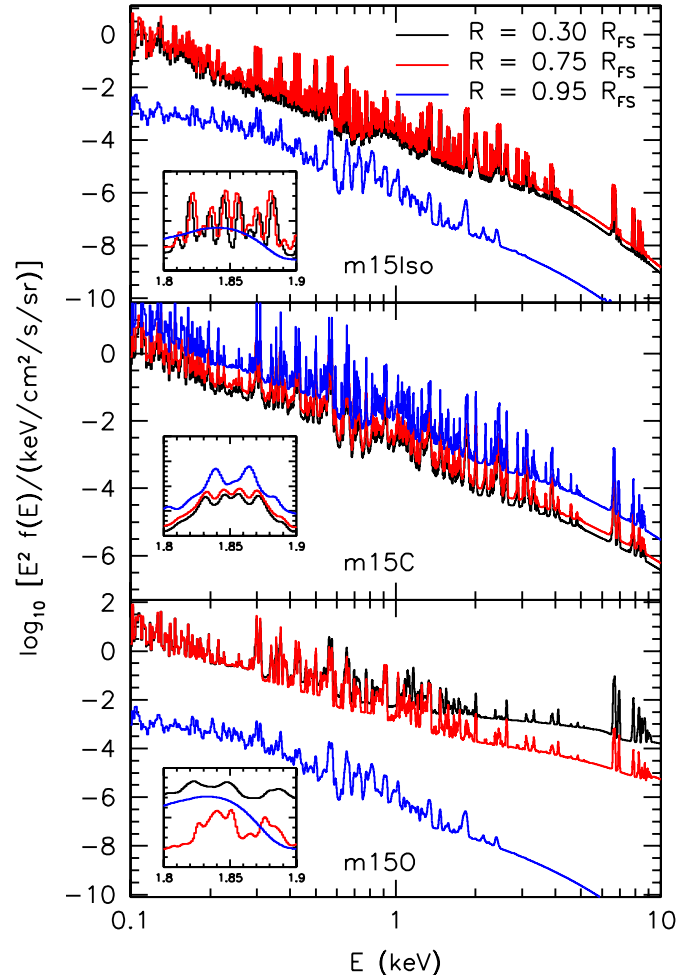


**Figure 9.** Integrated spectra for models **m15Iso** (top), **m15C** (middle) and **m150** (bottom), for projected radii of 0.3, 0.75, and  $0.95R_{\text{FS}}$ . Each radial extraction is of width  $dR/R_{\text{FS}} = 0.1$ . The inset regions show the line emission centered around Si XIII. For ease of comparison, the line profiles have been scaled by an arbitrary amount. The Doppler shifting of the line emission is seen most readily in models **m15Iso** and **m15C**. The red-shifted lines have not been corrected for absorption.

model **m150** is only  $\approx 2M_{\odot}$ . Additionally, as seen in Figure 2, exterior of  $R \approx 10R_{\odot}$ , the density of model **m150** is lower than that of either **m15C** or **m15Iso**. The progenitor of **m150** is not only more compact than the other models, but it also has a lower density envelope – the reverse shock can travel all the way into the center of the ejecta after only 400 years. At 400 years, model **m150** has already transitioned to the Sedov phase. This rapid transition is likely aided by the dense CSM shell.

In Figure 8 we plot the time evolution of the total thermal X-ray spectrum at  $t_{\text{SNR}} = 25, 200,$  and 400 years. For each model, we offset the spectrum from each epoch, for ease of comparison. We also show, inset, the evolu-

tion of the spectrum from 6-7 keV, without an offset. Even with the offset in the y-axis, the changes in the spectrum as the SNR evolves are apparent between the three models. In model **m150**, a sharp increase in Fe-L shell (Fe XVII – Fe XXIV) emission around 1 keV is seen after 200 years, while by 400 years, much of the Fe emission comes from K-shell emission. In contrast, as expected, there is a dramatic rise in the total X-ray emission in model **m150** between 25 and 200 years. Even after the shock breaks out of the shell, Fe-L shell and K-shell emission continue to increase over the remainder of the SNR’s evolution, probably as the reverse shock probes the deeper layers of the ejecta. This is best exemplified when contrasting the bottom row of Figure 7 with the righthand column of Figure 8: the X-ray emission from reverse shock heated material (red curves of Fig. 7) rises between 100 and 200 years, and only declines a bit over the next 200 years. In contrast, emission from shocked CSM drops steadily across the three epochs in these two models. The late time Fe emission shown in Figure 8 from model **m150** arises predominantly from shocked ejecta.

We plot the absolute line fluxes for K-shell emission in the inset panels of Figure 8, and list the centroid energies at  $t_{\text{SNR}} = 400$  years, in Table 2. Model **m150** results in a considerably higher line centroid at 400 years, than the other two models ( $\sim 10$  eV greater). As seen in the inset, the absolute line fluxes are nearly 2 orders of magnitude higher as well. This is expected – the blastwave has both swept up more material in the CSM **and** shocked more ejecta than the other models. The overall emission measure for model **m150** is higher, producing a higher overall flux, and the ionization timescale  $\tau = \int n_e(t)dt$  is much larger as well, resulting in a higher ionization state (see Figure 6).

Finally, in Figures 9 and 10, we plot the line of sight integrated spectra for three fiducial radii, and the projected 6.4-6.8 keV emissivity. We include both Doppler and thermal broadening in the spectral computations. At an age of 400 years, Doppler shifts are still detected towards the center of the SNR, allowing for discrimination between blue-shifted and red-shifted ejecta out to radii of  $0.75R_{\text{FS}}$ . We highlight emission around Si XIII. As seen in Figure 9, there does not appear to be any emission from this state of silicon in model **m15Iso** and **m150** at a radius of  $0.95R_{\text{FS}}$ . This is confirmed by the low charge state of silicon near the forward shock in these models, seen in the middle panel of Figure 6 (right), and in contrast to the much higher average charge state of silicon in model **m15C**.

For the line of sight Fe-K emission, models **m15Iso** and **m150** show expected profiles. Interior to the contact

interface, the Fe-K emission is dominated by emission from the reverse shock. Exterior to this, emission is from the shocked CSM only. In the case of model **m15C**, emission is primarily from forward shocked material everywhere. This is likely due to the strong interaction between the blastwave and the CSM shell. Interestingly, the reverse shock heated material is projected nearly to the forward shock. This is due to the fact that the forward shock is strongly decelerated in the shell. The radius of the contact interface in our model is  $0.93R_{\text{FS}}$ . For Figure 10, we choose extraction regions with resolution  $0.1R_{\text{FS}}$ . While the contact interface is very close to the forward shock, our choice of extraction binsize results in the outermost bin of shocked ejecta being projected to the radius of the forward shock.

### 3.2. Implications for Progenitor Identification

In the absence of a light echo spectrum which can be compared to template spectra for core collapse supernovae, relating a remnant back to its progenitor evolution remains tricky. As already discussed here, important mass loss processes can be triggered by several channels, including binary interaction and enhanced or episodic mass loss. Additionally, the once clear roadmap between progenitor and supernova type is more muddled, as supernovae are now observed to migrate between types as they evolve (e.g., Milisavljevic et al. 2015).

In specific terms, there have been several attempts to connect supernova remnants back to their progenitors. Most recently, Katsuda et al. (2015) detected thermal X-ray emission from the synchrotron dominated SNR RX J1713.7–3946. They found that the measured abundances favored a low mass progenitor, and that it likely lost much of its mass through binary interaction. This is at odds with previous work which considered a massive O star that carved out a large windblown bubble that the progenitor proceeded to explode into (e.g., Ellison et al. 2012).

More generally, Chevalier (2005) looked at the morphologies of several Galactic SNR, combined with qualities of their central compact objects, and typed several as IIPs, IILs, or IIbs, dependent upon the amount of mass estimated to have been lost during stellar evolution.

ChN has the capability to compute X-ray lightcurves. Dwarkadas & Gruszko (2012) compiled the lightcurves for all known X-ray supernovae, and showed that many deviate from the expected  $L_X \propto t^{-1}$  behavior. In Figure 11, we plot the 0.5–10 keV lightcurves for the three models. The lightcurves are distance and absorption independent.

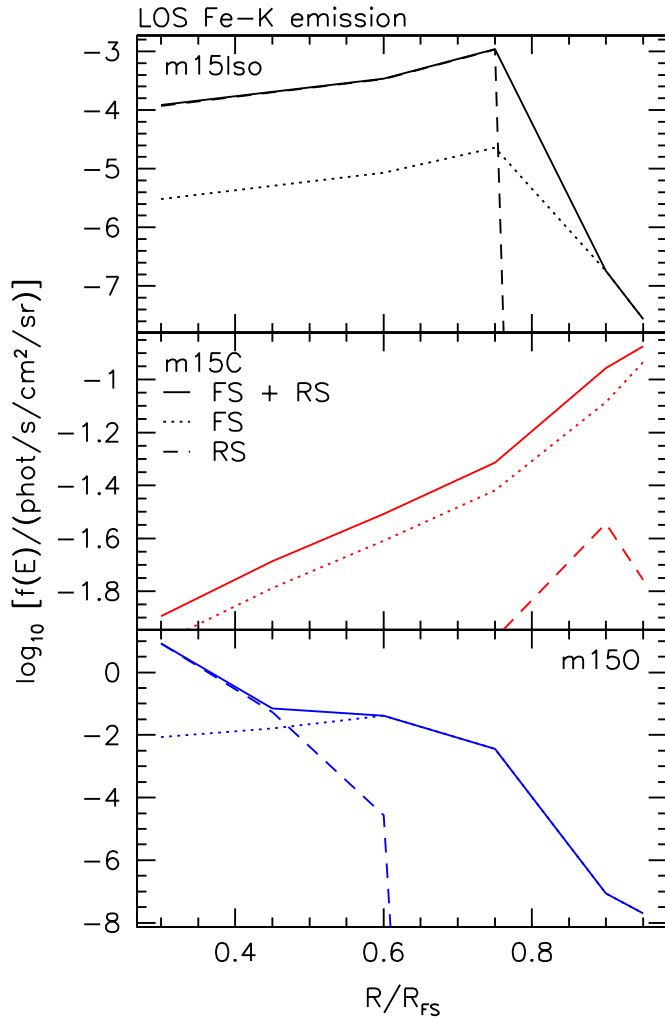


**Figure 10.** Line of sight projected emission from 6.4-6.8 keV, highlighting emission from Helium-like iron. The top panel corresponds to model *m15Iso*, the middle to *m15C*, and the bottom to *m150*. Each panel shows the contribution to the total flux from both the forward and reverse shock. In the case of model *m15C*, the shocked ejecta have caught up to the shocked CSM, as the forward shock moves through the CSM shell, over a radial distance that is unresolved by the choice of radial binning. All the plots have been normalized to the forward shock radii for each model.

As seen in Figure 11, there is a steady decline in the X-ray emission in model *m15Iso*, while the models with non-steady mass loss show different behavior - model *m150* shows a sharp increase in luminosity due to the early interaction between the blastwave and CSM shell, while model *m15C* follows model *m15Iso* closely before the shock-shell interaction. We have overlaid the current X-ray luminosity for select historical core collapse supernovae, as well as theoretical curves for the X-ray emission as a function of time for a range of mass loss

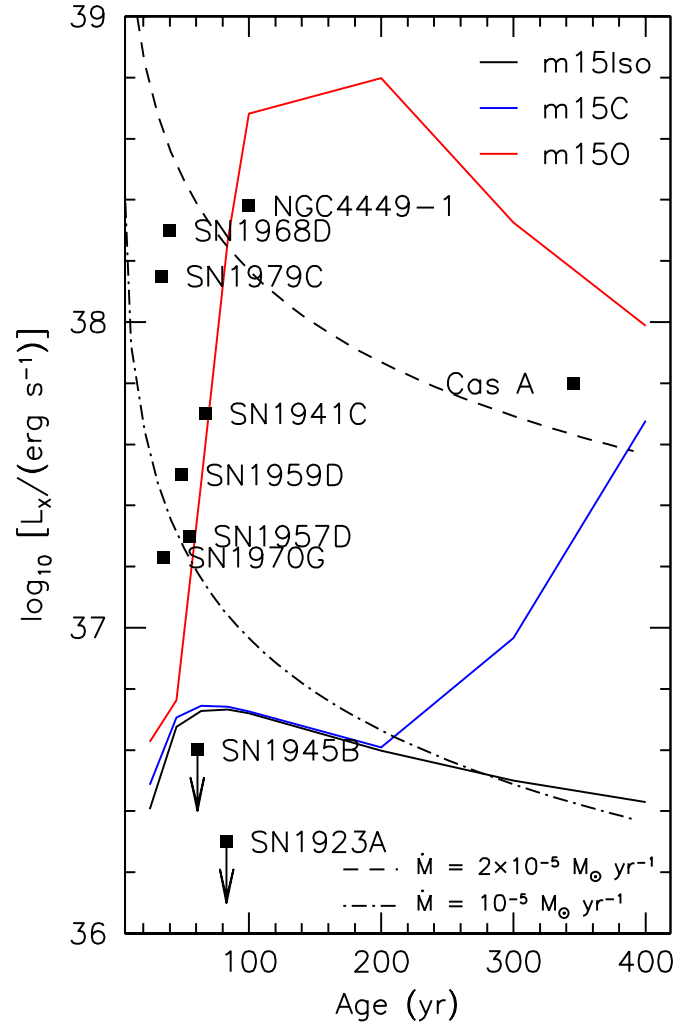


**Figure 11.** 0.5 - 10.0 keV X-ray luminosity for each model. Also shown are the approximate X-ray luminosities for several historical supernova remnants, as well as the expected X-ray luminosity due to free-free emission for mass loss rates of  $10^{-5}$  and  $2 \times 10^{-5} M_{\odot} \text{ yr}^{-1}$ , assuming isotropic mass loss (Immler & Lewin 2003). Data are taken from Patnaude & Fesen (2003); Stockdale et al. (2006); Soria & Perna (2008); Patnaude et al. (2011); Long et al. (2012); Ross & Dwarkadas (2017).

rates and wind velocities (Immler & Lewin 2003). While we are not aiming to model any particular SNR, it is worth noting that the data from any particular SNR are neither inconsistent with the luminosity predictions from our models, nor the predictions from self-similar models such as those shown in Figure 11.

Dwarkadas & Gruszko (2012) published historical lightcurves for 41 X-ray supernovae. They showed that the lightcurves do not decline as  $t^{-1}$  as would be expected from isotropic mass loss. They argued that some

of this is due to how the X-ray temperature changes as the blastwave evolves, resulting in differing *observed* emission as the peak of the emissivity function changes, but some of the trends they observe in the lightcurves may also be due to the structure of the circumstellar environment. The theoretical curves presented in Fig. 11 represent contributions from shocked CSM only, and do not account for the delayed rise in X-ray emission from shocked ejecta (c.f., Figure 1 right of Patnaude et al. 2015). Qualitatively, the luminosity in the isotropic mass loss models are similar to our models, but they assume a steady decline in the CSM density, which is clearly not the case for our models m15C and m150. Of additional interest are the large differences in luminosity between observations and our models (and the self similar models overplotted in Figure 11). As seen in Dwarkadas & Gruszko (2012), the X-ray luminosity for several of their supernovae varies between  $10^{38}$  and  $10^{40}$  erg s<sup>-1</sup> over the first few decades of supernova evolution. These observed luminosities are much higher than what we see in our models at early epochs. We interpret this as meaning that the mass loss rates are  $> 10^{-5} M_{\odot} \text{ yr}^{-1}$  prior to core collapse, or that dense CSM shells exist at radii  $< 10^{17}$  cm. Observations of recent and not-so recent SN support this (e.g., SN 1996cr, SN 2005kd, and SN 2014C; Dwarkadas et al. 2010, 2016; Margutti et al. 2017). Alternatively, the models presented here begin at an age of 5 years post core collapse. Choosing a starting age for our simulation closer to the time of core collapse would likely result in higher X-ray luminosities earlier in the evolution, in line with the self-similar predictions.

An interesting feature of Figure 11 is the gap of observational data between  $\sim 50$ – $100$  year old extragalactic remnants, and the  $\sim 340$  year old Cas A SNR. Remnants with ages of  $\sim 100$  years probe the mass loss history in the latter stages of the red supergiant phase, an interesting time in massive star evolution. Future X-ray observatories such as *Athena* will be able to access these epochs in young SNR such as SN 1957D and NGC 4449-1.

When comparing the X-ray light curves in Figure 11, it becomes clear that the integrated X-ray emission from a supernova or supernova remnant does not tell the full story. At any one epoch, dissimilar mass loss rates can give similar  $L_X$ 's. Examining the dynamics and the detailed ionization state of the gas will break the degeneracy. For instance, at ages of 400 years, model m15C and the self similar model with a steady  $2 \times 10^{-5} M_{\odot} \text{ yr}^{-1}$  differ in luminosity by less than 0.1 dex. At that age, m15C has a radius of 1.62 pc. In contrast, the blastwave radius for a 400 yr old SNR with constant mass loss is  $\sim 4$  pc (see Figure 1, right of Patnaude et al. 2015). From

Patnaude et al. (2015), the Fe-K luminosity for a model with mass loss rate of  $2 \times 10^{-5} M_{\odot} \text{ yr}^{-1}$  is estimated to be  $\lesssim 10^{42}$  photon s<sup>-1</sup>. The luminosity in the Fe-K line in model m15C is estimated to be  $\gtrsim 400 \times$  this. Even though the broadband X-ray luminosities between the models are quite close, the details of the dynamics and ionization balance of the shocked material tell a different story about how the blastwave interacted with the pre-supernova environment.

#### 4. CONCLUSIONS

We have presented the first quasi self-consistent models for the evolution of  $15M_{\odot}$  stars from the pre-main sequence through core collapse, and into the remnant phase. To our knowledge, this is the first attempt to produce such an end-to-end simulation in a self-consistent fashion. We have followed the evolution of the remnant to an age of 400 years, at which point one of our models, m150, has entered the Sedov phase. The only difference between the three models is the mass loss history of the progenitor. We find that the mass loss in late stages (during and after core carbon burning) can have a profound impact on the dynamics and spectral evolution of the supernova remnant. While our models are currently not tailored to any particular SN or SNR, we note that:

- Extreme mass loss during core neon or oxygen burning can result in CSM shells at distances  $> 0.5$  pc. While the shell is not in the immediate vicinity of the progenitor, the shock/shell interaction will leave its imprint on the emitted X-ray spectrum centuries after the shock has broken through the shell.
- Enhanced mass loss during post core helium burning phases can result in CSM shells at radii of less than a couple of parsecs. These shells are created only a few thousand years prior to core collapse. While we do expect them to collapse to thin shells due to radiative cooling, the shell will persist through progenitor core collapse. Depending upon the energetics, the blastwave will interact with the remnant of the shell up to a couple of hundred years after core collapse, resulting in an increase in X-ray emission from the shocked CSM. Our one-dimensional models, which do not follow in detail the dynamical and radiative evolution of the shell after its formation, which may lead to clumping or fragmentation of the shell, provide an upper limit on the amount of X-ray emission from the shock-shell interaction in this scenario.
- In Patnaude et al. (2015), we postulated that enhanced mass loss in the years leading up to core

collapse would result in increased X-ray emission, with little impact on the late time dynamics. Our simulations bear this out – CSM shells close to the progenitor result in a sharp increase in the X-ray emission up to a century after core collapse. However, once the shock breaks through the shell, it accelerates and the forward shock is dynamically similar to models with isotropic mass loss. We expect that this is due to the energetics of the explosion: in models with enhanced or extreme mass loss, the specific energy of the ejecta is higher than in the more massive model (by about a factor of 2). During the early phases of the remnant evolution, the blastwave dynamics are not strongly determined by the CSM structure, since the total mass in the ejecta is half that of the isotropic mass loss model. This argues that when considering the X-ray emission from supernova remnants, the mass loss history of the progenitor should be carefully considered. *Where* and *when* the mass was deposited in the CSM can have a profound impact on the evolution of the remnant.

Our models are not yet tailored to pinpoint the evolutionary history of any one supernova remnant. However, given the high fidelity data that currently exists for both evolved ( $t_{\text{SNR}} \sim 1000$  yr) and young ( $t_{\text{SNR}} \lesssim 100$  yr) SNRs, the progenitor mass loss history can be reconstructed with reasonable precision (see, e.g., Dwarkadas & Gruszko 2012). Thus, Galactic and extragalactic SNRs may now (or in the future) be probed as a class of objects. With the forthcoming advent of high spatial and spectral resolution microcalorimeters on missions such as *Athena* and *Lynx*, we can probe the progenitor evolution of extragalactic SNe and SNR by studying the detailed evolution of their spectra and comparing them to our evolutionary models.

The authors wish to thank Frank Timmes, H. Thomas Janka, Randall Smith, and Rob Fesen for fruitful discussions. D. J. P. acknowledges support from the *Chandra* Theory Program NASA/TM6-17003X, and NASA contract NAS8-03060.

## REFERENCES

- Blondin, J. M., & Lufkin, E. A. 1993, *ApJS*, 88, 589
- Castro, D., Slane, P., Ellison, D. C., & Patnaude, D. J. 2012, *ApJ*, 756, 88
- Chakraborti, S., Ray, A., Smith, R., et al. 2016, *ApJ*, 817, 22
- Chevalier, R. A. 2005, *ApJ*, 619, 839
- Chugai, N. N., & Chevalier, R. A. 2006, *ApJ*, 641, 1051
- Duffell, P. C. 2016, *ApJ*, 821, 76
- de Mink, S. E., Langer, N., Izzard, R. G., Sana, H., & de Koter, A. 2013, *ApJ*, 764, 166
- Dwarkadas, V. V. 2005, *ApJ*, 630, 892
- Dwarkadas, V. V. 2007, *ApJ*, 667, 226
- Dwarkadas, V. V., Dewey, D., & Bauer, F. 2010, *MNRAS*, 407, 812
- Dwarkadas, V. V., & Gruszko, J. 2012, *MNRAS*, 419, 1515
- Dwarkadas, V. V., Romero-Cañizales, C., Reddy, R., & Bauer, F. E. 2016, *MNRAS*, 462, 1101
- Elias-Rosa, N., Pastorello, A., Benetti, S., et al. 2016, *MNRAS*, 463, 3894
- Ellison, D. C., Patnaude, D. J., Slane, P., Blasi, P., & Gabici, S. 2007, *ApJ*, 661, 879
- Ellison, D. C., Patnaude, D. J., Slane, P., & Raymond, J. 2010, *ApJ*, 712, 287
- Ellison, D. C., Slane, P., Patnaude, D. J., & Bykov, A. M. 2012, *ApJ*, 744, 39
- Farmer, R., Fields, C. E., Petermann, I., et al. 2016, *ApJS*, 227, 22
- Foster, A. R., Ji, L., Smith, R. K., & Brickhouse, N. S. 2012, *ApJ*, 756, 128
- Fraser, M., Inserra, C., Jerkstrand, A., et al. 2013, *MNRAS*, 433, 1312
- Glebbeek, E., Gaburov, E., de Mink, S. E., Pols, O. R., & Portegies Zwart, S. F. 2009, *A&A*, 497, 255
- Immler, S., & Lewin, W. H. G. 2003, *Supernovae and Gamma-Ray Bursters*, 598, 91
- Janka, H.-T. 2012, *Annual Review of Nuclear and Particle Science*, 62, 407
- Kamble, A., Margutti, R., Soderberg, A. M., et al. 2016, *ApJ*, 818, 111
- Katsuda, S., Acero, F., Tominaga, N., et al. 2015, *ApJ*, 814, 29
- Kuncarayakti, H., Maeda, K., Anderson, J. P., et al. 2016, *MNRAS*, 458, 2063
- Lee, J.-J., Park, S., Hughes, J. P., et al. 2010, *ApJ*, 711, 861
- Lee, S.-H., Ellison, D. C., & Nagataki, S. 2012, *ApJ*, 750, 156
- Lee, S.-H., Slane, P. O., Ellison, D. C., Nagataki, S., & Patnaude, D. J. 2013, *ApJ*, 767, 20
- Lee, S.-H., Patnaude, D. J., Ellison, D. C., Nagataki, S., & Slane, P. O. 2014, *ApJ*, 791, 97



- Lee, S.-H., Patnaude, D. J., Raymond, J. C., et al. 2015, *ApJ*, 806, 71
- Li, H., McCray, R., & Sunyaev, R. A. 1993, *ApJ*, 419, 824
- Long, K. S., Blair, W. P., Godfrey, L. E. H., et al. 2012, *ApJ*, 756, 18
- Maeda, K., Hattori, T., Milisavljevic, D., et al. 2015, *ApJ*, 807, 35
- Margutti, R., Milisavljevic, D., Soderberg, A. M., et al. 2014, *ApJ*, 780, 21
- Margutti, R., Kamble, A., Milisavljevic, D., et al. 2017, *ApJ*, 835, 140
- Mauerhan, J. C., Smith, N., Filippenko, A. V., et al. 2013, *MNRAS*, 430, 1801
- Milisavljevic, D., Margutti, R., Soderberg, A. M., et al. 2013, *ApJ*, 767, 71
- Milisavljevic, D., Margutti, R., Kamble, A., et al. 2015, *ApJ*, 815, 120
- Morozova, V., Piro, A. L., Renzo, M., et al. 2015, *ApJ*, 814, 63
- Morozova, V., Piro, A. L., & Valenti, S. 2017, *ApJ*, 838, 28
- Nieuwenhuijzen, H., & de Jager, C. 1990, *A&A*, 231, 134
- Nugis, T., & Lamers, H. J. G. L. M. 2000, *A&A*, 360, 227
- Nymark, T. K., Fransson, C., & Kozma, C. 2006, *A&A*, 449, 171
- Ofek, E. O., Sullivan, M., Cenko, S. B., et al. 2013, *Nature*, 494, 65
- Ofek, E. O., Sullivan, M., Shaviv, N. J., et al. 2014, *ApJ*, 789, 104
- Ott, C. D., Burrows, A., Dessart, L., & Livne, E. 2008, *ApJ*, 685, 1069-1088
- Paczynski, B. 1983, *ApJ*, 267, 315
- Pastorello, A., Mattila, S., Zampieri, L., et al. 2008, *MNRAS*, 389, 113
- Pastorello, A., Cappellaro, E., Inzerra, C., et al. 2013, *ApJ*, 767, 1
- Patnaude, D. J., & Fesen, R. A. 2003, *ApJ*, 587, 221
- Patnaude, D. J., Ellison, D. C., & Slane, P. 2009, *ApJ*, 696, 1956
- Patnaude, D. J., Slane, P., Raymond, J. C., & Ellison, D. C. 2010, *ApJ*, 725, 1476
- Patnaude, D. J., Loeb, A., & Jones, C. 2011, *NewA*, 16, 187
- Patnaude, D. J., Lee, S.-H., Slane, P. O., et al. 2015, *ApJ*, 803, 101
- Patnaude, D., & Badenes, C. 2017, arXiv:1702.03228
- Paxton, B., Bildsten, L., Dotter, A., et al. 2011, *ApJS*, 192, 3
- Paxton, B., Cantiello, M., Arras, P., et al. 2013, *ApJS*, 208, 4
- Paxton, B., Marchant, P., Schwab, J., et al. 2015, *ApJS*, 220, 15
- Piro, A. L., & Morozova, V. S. 2016, *ApJ*, 826, 96
- Podsiadlowski, P., Joss, P. C., & Hsu, J. J. L. 1992, *ApJ*, 391, 246
- Quataert, E., & Shiode, J. 2012, *MNRAS*, 423, L92
- Ross, M., & Dworkadas, V. V. 2017, *AJ*, 153, 246
- Shiode, J. H., & Quataert, E. 2014, *ApJ*, 780, 96
- Slane, P., Lee, S.-H., Ellison, D. C., et al. 2014, *ApJ*, 783, 33
- Smith, N. 2014, *ARA&A*, 52, 487
- Smith, N., & Arnett, W. D. 2014, *ApJ*, 785, 82
- Smith, N., Mauerhan, J. C., & Prieto, J. L. 2014, *MNRAS*, 438, 1191
- Smith, N., Kilpatrick, C. D., Mauerhan, J. C., et al. 2017, *MNRAS*, 466, 3021
- Soria, R., & Perna, R. 2008, *ApJ*, 683, 767-772
- Stockdale, C. J., Maddox, L. A., Cowan, J. J., et al. 2006, *AJ*, 131, 889
- Sutherland, R. S., & Dopita, M. A. 1993, *ApJS*, 88, 253
- Timmes, F. X., & Swesty, F. D. 2000, *ApJS*, 126, 501
- Truelove, J. K., & McKee, C. F. 1999, *ApJS*, 120, 299
- Vink, J. S., de Koter, A., & Lamers, H. J. G. L. M. 2001, *A&A*, 369, 574
- Wongwathanarat, A., Müller, E., & Janka, H.-T. 2015, *A&A*, 577, A48
- Wongwathanarat, A., Janka, H.-T., Müller, E., Pllumbi, E., & Wanajo, S. 2017, *ApJ*, 842, 13
- Yoon, S.-C., & Cantiello, M. 2010, *ApJL*, 717, L62
- Young, P. A., & Fryer, C. L. 2007, *ApJ*, 664, 1033

**Table 1.** MESA Initial and Final Model Parameters

Model	$M_{\text{Final}}$	$M_C$	$M_O$	$M_{Si}$	$M_{Fe}$	R	$\dot{M}^a$
			$M_{\odot}$			$\log_{10} R/R_{\odot}$	$M_{\odot} \text{ yr}^{-1}$
m15Iso	13.3	2.56	2.48	1.70	1.53	2.99	$5 \times 10^{-6}$
m15C	10.0	2.56	2.49	1.68	1.51	3.03	$10^{-4}$
m15O	5.7	2.56	2.46	1.69	1.53	2.93	0.1

<sup>a</sup>Mass loss rates are given for the time period of interest. For the isotropic case, the average mass loss rate of  $5 \times 10^{-6} M_{\odot} \text{ yr}^{-1}$  is used.

**Table 2.** ChN Dynamical and Spectral Results at  $t_{\text{SNR}} 400 \text{ yr}$ 

Model	$R_{\text{FS}}$	$M_{\text{ej}}$	$M_{\text{swept up}}$	He-like Fe
	pc	$M_{\odot}$	$M_{\odot}$	keV
m15Iso	1.99	2.0	0.6	6.662
m15C	1.62	6.0	2.4	6.665
m15O	1.98	5.9	8.6	6.676